https://doi.org/10.5194/wes-2026-112
Preprint. Discussion started: 14 July 2026


WIND ENERGY SCIENCE DISCUSSIONS
Open Access
european academy of wind energy

# Implementing raceway damage in a finite-element blade bearing model

Matthis Graßmann[1], Oliver Menck[1], Apoorva Avinash Kulkarni[1], Florian Schleich[1]

[1] Fraunhofer Institute for Wind Energy Systems IWES, Large Bearing Laboratory, Am Schleusengraben 22, 21029 Hamburg, Germany

*Correspondence to*: Matthis Graßmann (matthis.grassmann@iwes.fraunhofer.de)

**Abstract.**

During the operation of large slewing bearings, material outbreaks on the raceway due to rolling contact fatigue can occur. These local raceway damages can lead to unloaded rolling elements because of changes in the surface geometry and with that alter the internal load distribution and thus significantly affect the remaining service life of the bearing. While finite-element (FE) models are widely used to determine load distributions, the influence of such damage on the global bearing behavior has not yet been sufficiently addressed. In this work, a methodology to implement raceway damage in a finite-element model of a downscaled double-row four-point contact ball blade bearing is presented. To ensure computational efficiency, the ball–raceway interactions are represented by nonlinear spring elements, which are extended by pretension elements to introduce local gaps corresponding to measured damage depths. The damage progression on the raceways of rolling contact fatigue tests is documented and considered in the FE simulations. The resulting deformation behavior is validated by comparing simulation and experimental. strain gauge data on the bearing outer rings. The comparison shows that the model can reproduce the characteristic changes in the bearing behavior caused by increasing damage, with good agreement for most investigated states. The simulations further reveal that local material removal leads to pronounced changes in the global load distribution, including load increases on adjacent balls. Bearing life calculations based on the altered global load distributions indicate a negative influence on the service life. The results highlight the importance of considering damage-induced load redistribution when assessing the condition and residual life of wind turbine blade bearings in operation.

## 1 Introduction

Large slewing bearings with diameters of several meters are essential components in wind turbines, cranes, and other heavy-duty applications. In wind turbines, blade bearings connect the rotor blade to the hub and enable controlled pitch motion under highly dynamic loading conditions. These bearings are subjected to high alternating loads and oscillatory movements, resulting in complex internal load distributions and deformation patterns. During their operation, material outbreaks can appear on the raceways, for example due to rolling contact fatigue. Fatigue tests show that ball bearings can operate further

https://doi.org/10.5194/wes-2026-112
Preprint. Discussion started: 14 July 2026


even with raceway damage (Rumbarger 1969; Kotzalas and Harris 2001; Rosado et al. 2009; Behnke and Menck 2025). However, the remaining service life of the bearing changes constantly with increasing damage because of changes in the distribution of ball forces and resulting contact pressures. Accurate knowledge of these load distributions is crucial for reliable design and lifetime prediction as well as ongoing service life evaluation of the bearing. Finite-element analysis (FEA) is currently the only viable approach to determine the load distribution and changes in the bearing behavior due to damage (Stammler et al. 2024).

Different approaches of creating FE rolling bearing models to obtain the internal load distribution of the rolling elements have been published (Daidié et al. 2008; Aguirrebeitia et al. 2012; Chen and Wen 2012; Gao et al. 2011; Smolnicki and Rusiński 2007; Liu et al. 2018; Wang et al. 2017; Stammler et al. 2018; Graßmann et al. 2026). Researchers have been using these approaches to investigate the influence of manufacturing tolerances of rolling elements and raceways as well as bearing characteristics like clearance on the resulting load distribution (Potočnik et al. 2013; Heras et al. 2019a; Heras et al. 2019b; Starvin and Manisekar 2015; Aithal et al. 2015). Furthermore, single contact FE models have been developed to investigate subsurface-initiated spalling to predict the rolling contact fatigue life of a bearing (Walvekar et al. 2017; Slack and Sadeghi 2010; Golmohammadi et al. 2018; Walvekar et al. 2018; Shen and Zhou 2019). SINGH et al. (2014; 2018) created a two-dimensional FE model of a ball bearing with an outer diameter of 220 mm to investigate the effect of a rectangular defect on the outer raceway on the vibration response of the bearing. They implemented a spall with a length of 10 mm and a depth of 0.2 mm and simulated the bearing with a radial load of 50 kN and a rotational speed of 500 RPM. They discovered characteristics in their data that represent the unloading and reloading of a rolling element traveling through the damaged area on the raceway. OHANA et al. (2022) created a two-dimensional single contact model of a ball bearing with an outer diameter of 62 mm. They investigated the resulting stress and strain beneath the surface when the ball is in contact with the edge of a spall. They simulated different spall sizes and discovered two areas with tensile stresses that favor damage progression. BRANCH et al. (2010) and ARAKERE et al. (2009) created a three-dimensional single contact model of a ball bearing with a pitch diameter of 60.24 mm. They implemented a spall with a depth of 125 µm on the raceway and ran multiple static load analysis with different locations of the ball with respect to the damage. Their main result of the FE simulations is a drastic pressure increase on the spall's edges of up to 7.8 GPa.

In previous work, GRAßMANN et al. (2023) introduced a new modelling approach for FE bearing models where the ball-raceway interactions again are represented by nonlinear spring elements. But in contrast to other publications these springs are connected to the raceways by deformable force-distributed constraints allowing for a more realistic deformation of the bearing rings. They validated the FE model of a downscaled blade bearing with 750 mm outer diameter by comparing strain gauge values on the outer ring against experimental data of 4 different test rig assemblies. They achieved deviations of less than 10%. GRAßMANN et al. (2024) further investigated the influence of anomalies like dents, bulges, and inclined flanges on the surface of surrounding structures on the behavior of the bearing. They showed significant changes in the deformation of the bearing rings as well as the load distribution caused by anomalies within manufacturing tolerances.

The authors have defined two criteria for a successful validation of finite element slewing bearing models:

https://doi.org/10.5194/wes-2026-112
Preprint. Discussion started: 14 July 2026


- For the maximum strain, the FE results should deviate less than 10 % from the experimental data.
- The characteristic course (number and position of maxima and minima) of the FE results should match the experimental mean values.

None of the mentioned publications implement local material outbreaks on the raceways in the FE model to investigate the influence of raceway damage on the load distribution of the full bearing. It is to be expected that the load distribution across the entire bearing will change as soon as there is damage to the raceway. Any life calculation estimates the bearing life based on undamaged conditions. However, as soon as damage occurs the remaining service life highly depends on the actual load distribution in the bearing. Hence, changes in the load distribution while the bearing operates must be considered to determine changes in the calculated bearing life. This work introduces a methodology to consider raceway damage in FE bearing models and analyses changes in the load distribution and recalculates the bearing life to predict the likelihood of new damage initiation based on the altered bearing behavior. Sect. 2 describes the methodology including the test set up, damage evaluation, and life calculation. The results are presented and discussed in Sect. 3. Sect. 4 concludes this work and ends with an outlook for future work.

## 2 Methodology

### 2.1 Bearings and bearing models

The bearings investigated in this study are grease-lubricated double-row four-point contact ball bearings, exemplarily shown in Figure 1. They are downscaled blade bearings that are manufactured using the same production processes as full-scale blade bearings. All bearings considered in this work were produced on identical machines, under the same tolerance requirements, using the same material, and with identical specifications for the supporting structures. In contrast to smaller bearings used in typical industrial applications, large slewing bearings are not through-hardened but are surface-hardened by induction. The bearing is mounted to the surrounding structures through bore holes. The main geometrical parameters of the bearings are summarized in Table 1. While they have the same outer dimensions their main difference is the initial contact angle of 45° for the bearing 0411 and 35° for the bearing 0498. Further, bearing 0498 has a significantly higher torque under unloaded conditions which is most likely due to a higher system preload than bearing 0411. The use of downscaled blade bearings offers substantial advantages, as they are considerably more cost-effective and easier to handle than full-scale bearings. This enables a higher number of experimental investigations and, consequently, the creation of a more extensive database, which is particularly beneficial for the validation of FE models.

A defining characteristic of four-point contact ball bearings is their nominal contact angle of less than 90°. As a result, any external load induces ball forces with both axial and radial components, leading to a tilting of the bearing rings. With increasing load, the contact angle increases, which may result in truncation. Truncation describes the situation in which the theoretical contact ellipse extends beyond the edge of the raceway. This leads to locally increased contact pressures at the

https://doi.org/10.5194/wes-2026-112
Preprint. Discussion started: 14 July 2026


raceway edge, which may exceed the maximum theoretical contact pressure associated with a fully supported contact. Figure 1 shows the diagonals that carry the loads with an initial contact angle of 45°.

In the FE model used in this study, the interactions between the balls and the raceways are represented by nonlinear spring elements. These springs are positioned between opposing centers of curvature of the raceways, such that two springs form the diagonals responsible for transferring the load of a single ball. Force-distributed constraints (FDCs) are used to connect the springs to the raceways. Figure 2 exemplarily illustrates the FE mesh of the bearing rings for the bearing 0411 and the implemented ball–raceway contact modeling approach. The nonlinear springs are depicted in orange, the raceways connected to the springs in green, and the FDCs in blue. A detailed description of the modelling approach to create the FE bearing model, along with a verification of its plausibility, is provided in (Graßmann et al. 2023). In that work, the behavior of the FE bearing model is validated against extensive experimental data. To implement raceway damage to the bearing model, pretension elements are added to every nonlinear spring element that represents the ball-raceway interactions. Each pretension element can individually be loaded with a force or a displacement allowing it to function as a gap element. Figure 3 shows the initial nonlinear spring element connecting the opposing centers of the raceways 1 and 1' on the left. On the right, it shows the spring-pretension combination with the additional node 2. Applying a negative displacement between node 1 and 2 defines a gap (exaggerated indicated by the dashed lines) which must be overcome before the spring carries any load.

**Table 1: Main dimensions of the bearings**

| Property | Symbol | Value | | Unit |
|---|---|---|---|---|
| | | ID 0411 | ID 0498 | |
| Inner diameter | - | 596 | 596 | mm |
| Outer diameter | - | 750 | 750 | mm |
| Pitch diameter | $d_m$ | 673 | 673 | mm |
| Inner bolt circle diameter | IBCD | 621 | 621 | mm |
| Outer bolt circle diameter | OBCD | 725 | 725 | mm |
| Total height | h | 92 | 92 | mm |
| Ball diameter | D | 25.4 | 20 | mm |
| Balls per row | Z | 69 | 72 | - |
| Rows | i | 2 | 2 | - |
| Inner ring bolts | - | 72 | 72 | - |
| Outer ring bolts | - | 72 | 72 | - |
| Nominal contact angle | α | 45 | 35 | ° |
| Groove conformity | $f_i$, $f_e$ | 0.53 | 0.54 | - |
| Mass | m | 92.66 | 90.00 | kg |

https://doi.org/10.5194/wes-2026-112
Preprint. Discussion started: 14 July 2026

eawe european academy of wind energy
Open Access WIND ENERGY SCIENCE DISCUSSIONS

| | | | | |
|---|---|---|---|---|
| Torque | T | 185 | 660 | Nm |


**Figure 1: Double-row four-point contact ball bearing (left) (© Fraunhofer IWES/Ulrich Perrey) and load carrying diagonals (right).**

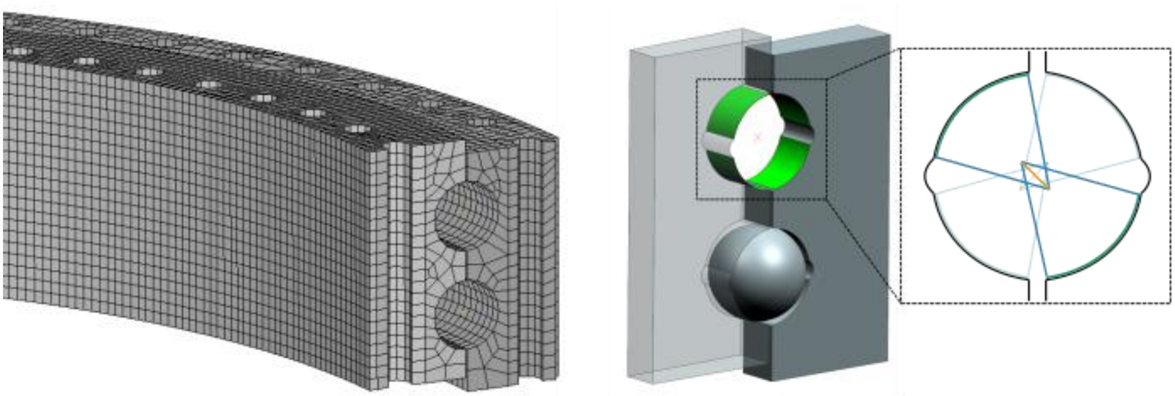

**Figure 2: Mesh of the bearing model and modelled ball-raceway contact with nonlinear springs connected to the raceways via FDCs (Graßmann et al. 2023).**

https://doi.org/10.5194/wes-2026-112
Preprint. Discussion started: 14 July 2026


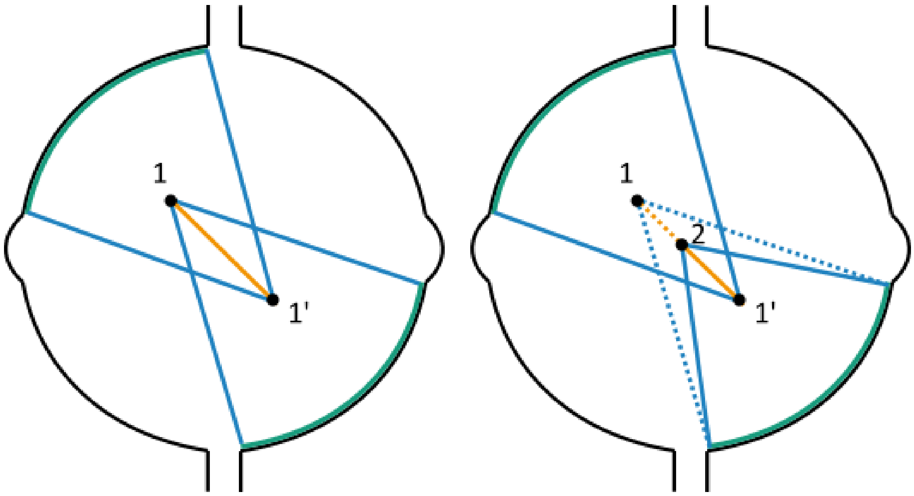


Figure 3: Ball raceway interaction modelled with nonlinear spring (left) and spring-pretension combination with exaggerated applied gap (right)

### 2.2 Test environment and FE model

The experimental investigations were conducted on the BEAT1.1 test rig (Bearing Endurance and Acceptance Test rig), illustrated in Figure 4 (left). The test rig is designed to simultaneously test two bearings with diameters ranging from 400 mm to 800 mm. Load application is realized by six hydraulic cylinders arranged in a hexapod configuration and an electrical pitch actuator, enabling controlled loading in all six degrees of freedom. The test rig comprises a reaction frame at the bottom and a load platform at the top, which transfers the applied forces and moments to the bearings. Adapter rings connect the outer rings of the bearings to these structural components. The inner ring of the lower bearing is connected to a stiffener plate and a gear ring, which couples the rotating inner section of the test rig to an electric pitch motor. A force-transmitting element (FTE) links the inner rings of both bearings, thereby completing the load path within the test assembly. The BEAT1.1 test rig can apply static axial loads of up to 500 kN in tension and 1,000 kN in compression, as well as bending moments of up to ±250 kNm. When a bending moment is applied, the bearing experiences distinct traction and compression zones.

A FE model of the BEAT1.1 test rig was developed and includes the primary structural components. The hydraulic cylinders are represented by linear actuator elements. A cross-sectional view of the FE model with the integrated bearings is shown in Figure 4 (right). The reaction frame and load platform are shown in grey, the adapter rings in dark blue, the FTE in light blue, the gear ring in light grey, the stiffener plate in yellow, and the bearings in orange. The hydraulic cylinders are highlighted in red. The inner components connecting the bearing inner rings are joined by bolted connections. All surface contacts are defined as frictional, using a friction coefficient of 0.15 for steel-to-steel interfaces (Graßmann et al. 2023). This also applies to the contacts between the bearing outer rings and the adapter rings, ensuring a realistic representation of the deformation behavior of both bearings. The bolts are modeled using beam elements. In the simulation procedure, the bolts are tightened in an initial load step before the hydraulic loads are applied in a subsequent step. The target bolt pretension is

https://doi.org/10.5194/wes-2026-112
Preprint. Discussion started: 14 July 2026


40.6 kN. For the bearing 0498 additional stiffener plates are attached to the inner and outer rings of the bearings to reduce ring tilting and prevent truncation. These additional stiffening components are not displayed in the figure, however, they are considered in the FE simulations for this bearing.

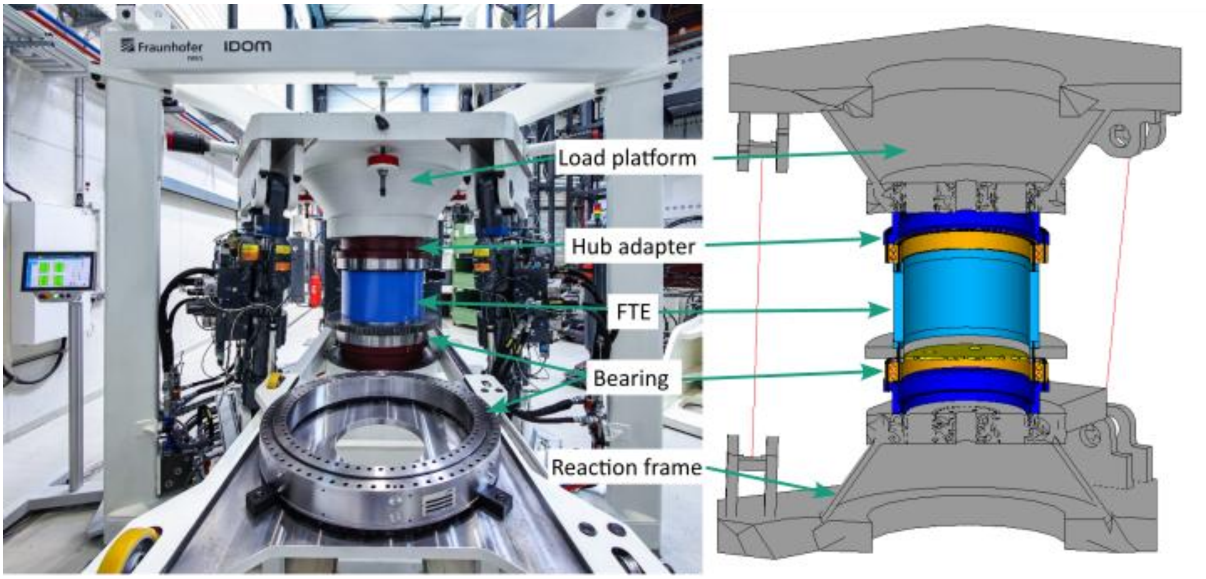


**Figure 4: Test rig BEAT1.1 with double-row four-point contact ball bearing (©Fraunhofer IWES/Ulrich Perrey) (left) and a cross-sectional view of the test rig FE model (right) (Graßmann et al. 2024).**

To ensure the reliability of the FE models, strain gauges are attached to the bearing outer rings to compare the bearing behavior in both undamaged and damaged states against experimental data. Strain gauges detect changes in electrical resistance caused by mechanical strain, allowing the local strain to be quantified. In total 12 strain gauges are equidistantly positioned around the circumference on the surface of the outer rings near the free flange at both bearings beginning at 25°. The strain gauges measure tangential strain, enabling the detection of ovalization of the bearing rings. Figure 5 illustrates the arrangement of the strain gauges on the outer bearing rings.

https://doi.org/10.5194/wes-2026-112
Preprint. Discussion started: 14 July 2026


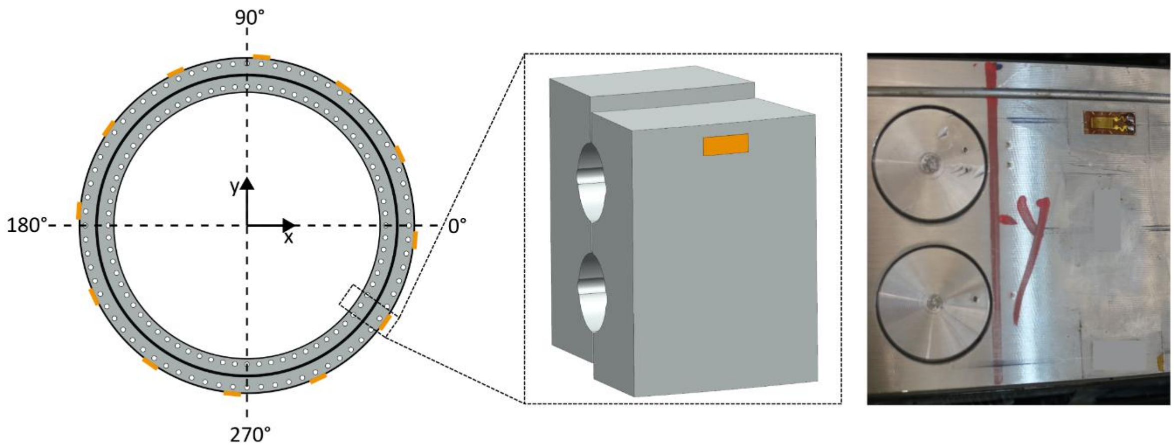


**Figure 5: Position of the strain gauges at the outer ring of the lower bearings.**

To enable a direct comparison between experimental and numerical results, the strain at the same locations is evaluated in the FE bearing model. For this purpose, virtual strain gauges are implemented by means of shell elements without stiffness, each representing one physical strain gauge. These shell elements are placed on the surface of the outer ring and are connected to existing mesh nodes. After completion of the simulation, the mean strain of each shell element is extracted and used for comparison with the experimental measurements.

### 2.3 Raceway fatigue tests

The raceway fatigue tests aim at testing rolling contact fatigue. Two different tests were conducted with the two bearings. The test for bearing 0411 applies 1,000 kN of pure axial compression force and then rotates 720° back and forth with a maximum speed of 52°/s. The test was stopped repeatedly to remove the bearing from the test setup, open it, and document the damage on the raceway. Then the bearing was reassembled and installed in the test rig again to restart the test. During this process as much of the old grease as possible was collected and put back into the bearing to keep lubrication conditions as similar as possible for the resumed test. After each reassembly, tests with bending moments capture strain gauge data as reference for FE simulations. The reference test applies -125 kNm bending moment and pitches the bearing inner ring from 0° to -60° and back. In total, the bearing was disassembled 6 times. As the test ended because the pitch drive could not rotate the bearing anymore, strain gauge data is only available for the bearing conditions of the first 5 dissassemblies. The damage in the bearing is more pronounced on the inner ring than on the outer ring. Figure 6 shows the damage progression on the inner ring of bearing 0411 at 180° from the 1$^{st}$ disassembly at the top left to the 6$^{th}$ disassembly at the bottom right. It shows damage initiation on the blade side row at 175° and 185° at the 1$^{st}$ disassembly. Then both damage marks keep growing during the tests until they merge at the 4$^{th}$ disassembly. At the 4$^{th}$ and 5$^{th}$ disassembly damage initiation is also visible at the hub side row. Finally, at the 6$^{th}$ disassembly, the damage covers the whole area of the shown raceway between 165° and 195° on both blade side and hub side row.

https://doi.org/10.5194/wes-2026-112
Preprint. Discussion started: 14 July 2026


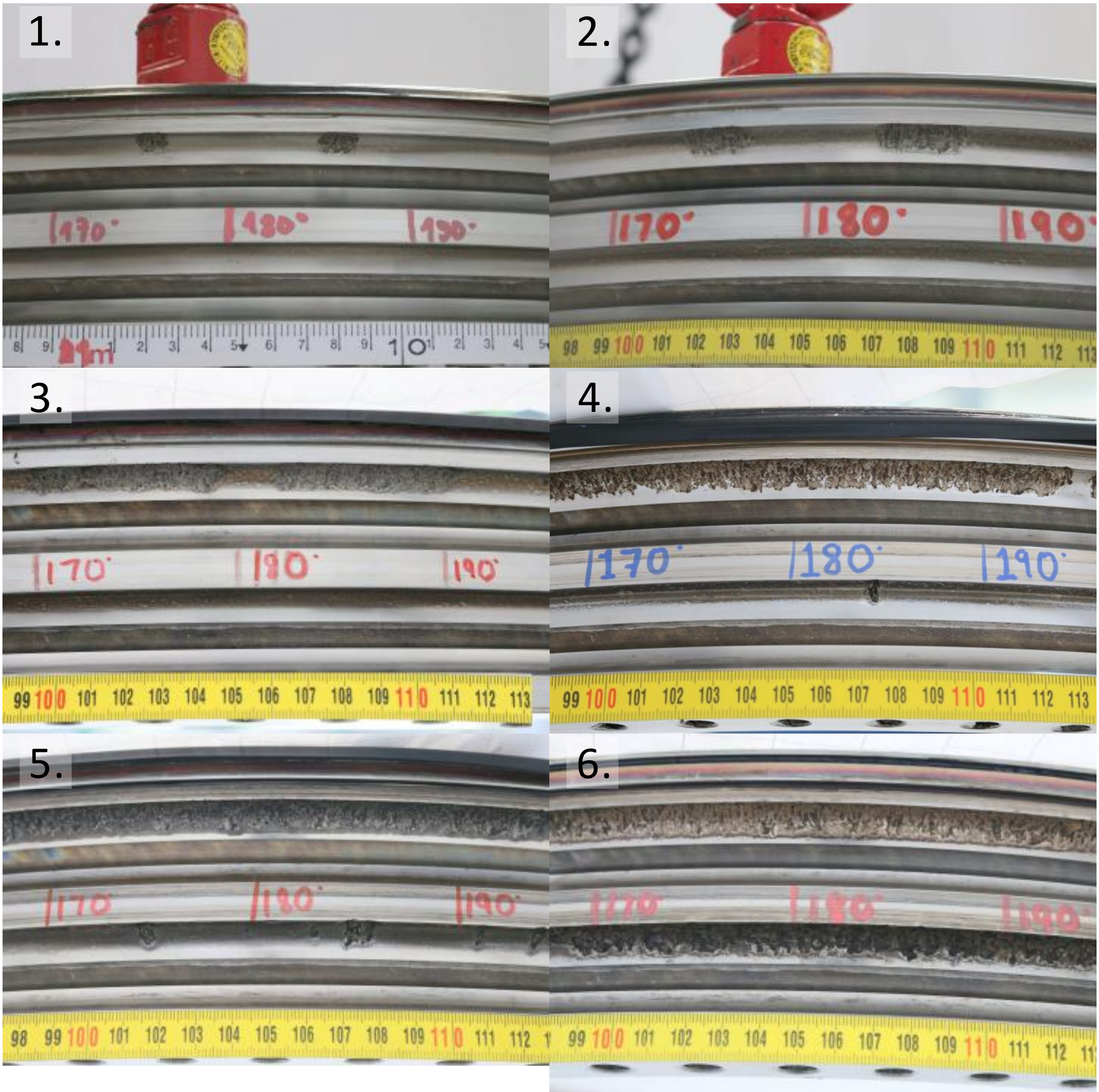


**Figure 6: Damage progression on the inner ring of bearing 0411 at 180° (Menck and Geibel 2025) ©Fraunhofer IWES/Oliver Menck, Deva Narayanan**

To quantify the damage progression, the bearing raceways are divided into equidistant segments according to the number of balls. Then each segment is defined as damaged when at least half of the raceway in this segment is covered with material outbreaks on either the inner or the outer ring. Figure 7 shows the damage progression of bearing 0411 for the blade side row

https://doi.org/10.5194/wes-2026-112
Preprint. Discussion started: 14 July 2026

Wind Energy Science Discussions

(left) and the hub side row (right). Due to the pure axial loading during the fatigue test only the diagonals 1 and 3 carry load and therefore are damaged. It shows that for the first four disassemblies the damage primarily progresses on the blade side row. At the fifth disassembly the hub side row has almost as many damaged areas as the blade side row and after the sixth disassembly the hub side row has even larger damage with more than half the raceway gone. It also shows that some damage marks start right away to grow while others remain constant in size over a long period of time. The damage in segment 13 on the blade side for example was first discovered at the second disassembly and it only became larger in the last examination of the bearing. The damage at 180° shown in Figure 6 originated in segments 35 and 37 in Figure 7. As the initial damage marks after the $1^{st}$ disassembly are not large enough to cover 50% of the segments, they are only considered from the $2^{nd}$ disassembly on for the FE simulations.

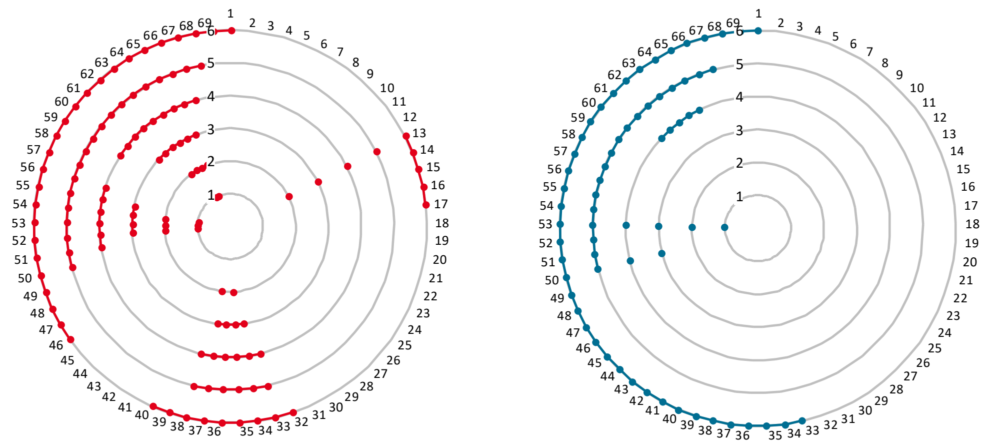


**Figure 7: Damage progression of bearing 0411 on the blade side row (left) and hub side row (right).**

The test for bearing 0498 applies a bending moment of 210 kNm and pitches the bearing with a double amplitude of 80° at a maximum speed of 52°/s. During the test the bearing was frequently inspected through the fill plugs to detect any damage on the inner ring. It was opened twice to fully document the damage. The first time only three segments on raceway 1 were damaged. The second disassembly documents the bearing condition after the test stopped when the electrical pitch drive could not turn the bearing anymore due to raceway damage. Reference tests at the beginning of the fatigue test and before each disassembly capture strain gauge data to compare the bearing behavior with the FE results. Figure 8 shows the damage on the different diagonals on the blade side (left) and hub (right) after the end of the fatigue test. Figure 9 exemplarily shows damage on the inner ring of bearing 0498 at 80° and 280°.

https://doi.org/10.5194/wes-2026-112
Preprint. Discussion started: 14 July 2026


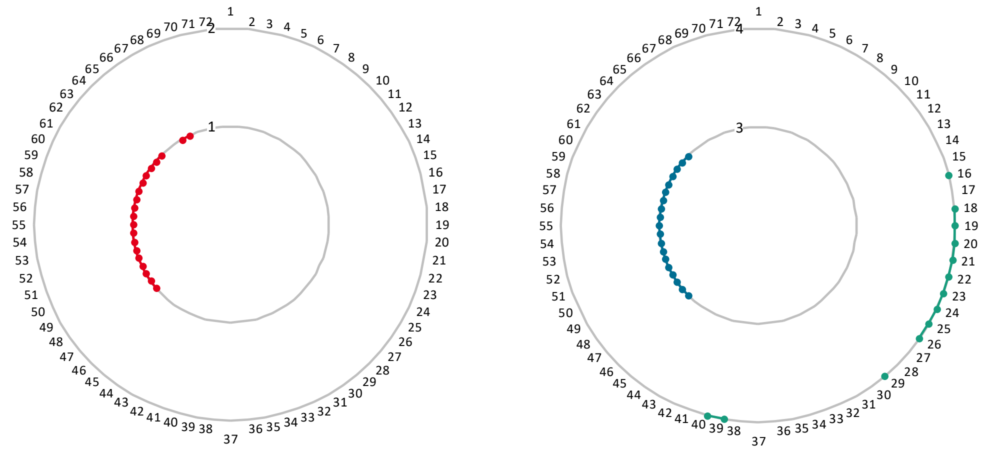


**Figure 8: Damage of bearing 0498 on diagonals 1 and 2 on the blade side row (left) and diagonals 3 and 4 on the hub side row (right) at the end of the test**

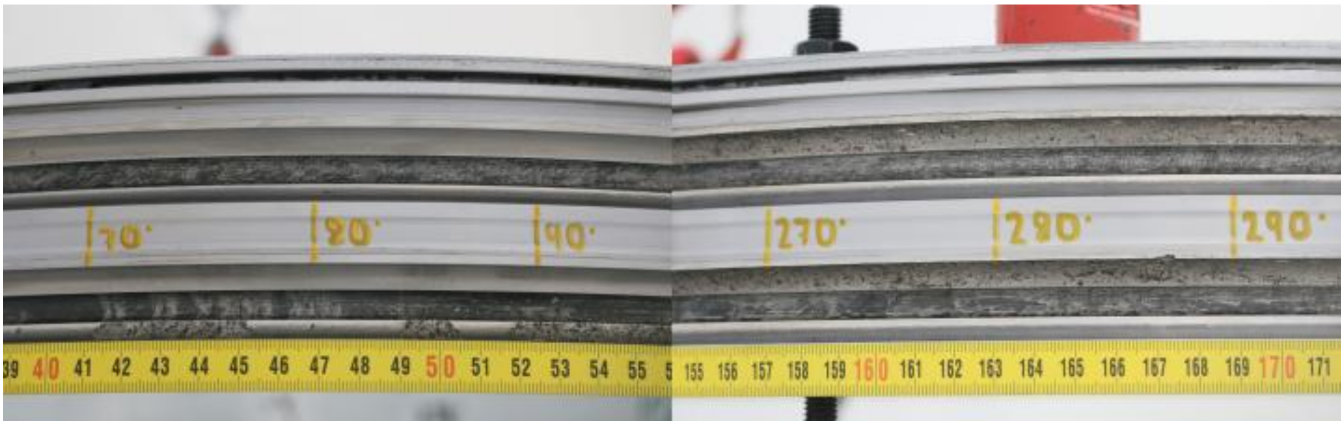


**Figure 9: Damage on the inner ring of bearing 0498 at 80° and 280° ©Fraunhofer IWES/Oliver Menck, Deva Narayanan**

### 2.4 Damage evaluation

Damage marks at different locations and during different disassemblies have been analyzed using a laser scanning microscope. Casting compound forms an imprint of the damaged area and allows for detailed measurements under the microscope. Because casting compound is used, any material removal appears as hills when the results are plotted. The scans show two different characteristic shapes of the damage marks: One with almost the same depth over the full mark and the other with different levels of depth. Figure 10 exemplarily shows the two characteristics of the damage marks of bearing 0411. The left scan shows the topology of the left damage mark at 225°. It shows a constant depth of approximately 200 µm over the full length of the mark. The right scan shows the topology of the larger damaged area between 330° and 340°. It shows multiple plateaus at different depths. However, the first plateau which would be in contact with the ball first is at roughly 200 µm.

https://doi.org/10.5194/wes-2026-112
Preprint. Discussion started: 14 July 2026




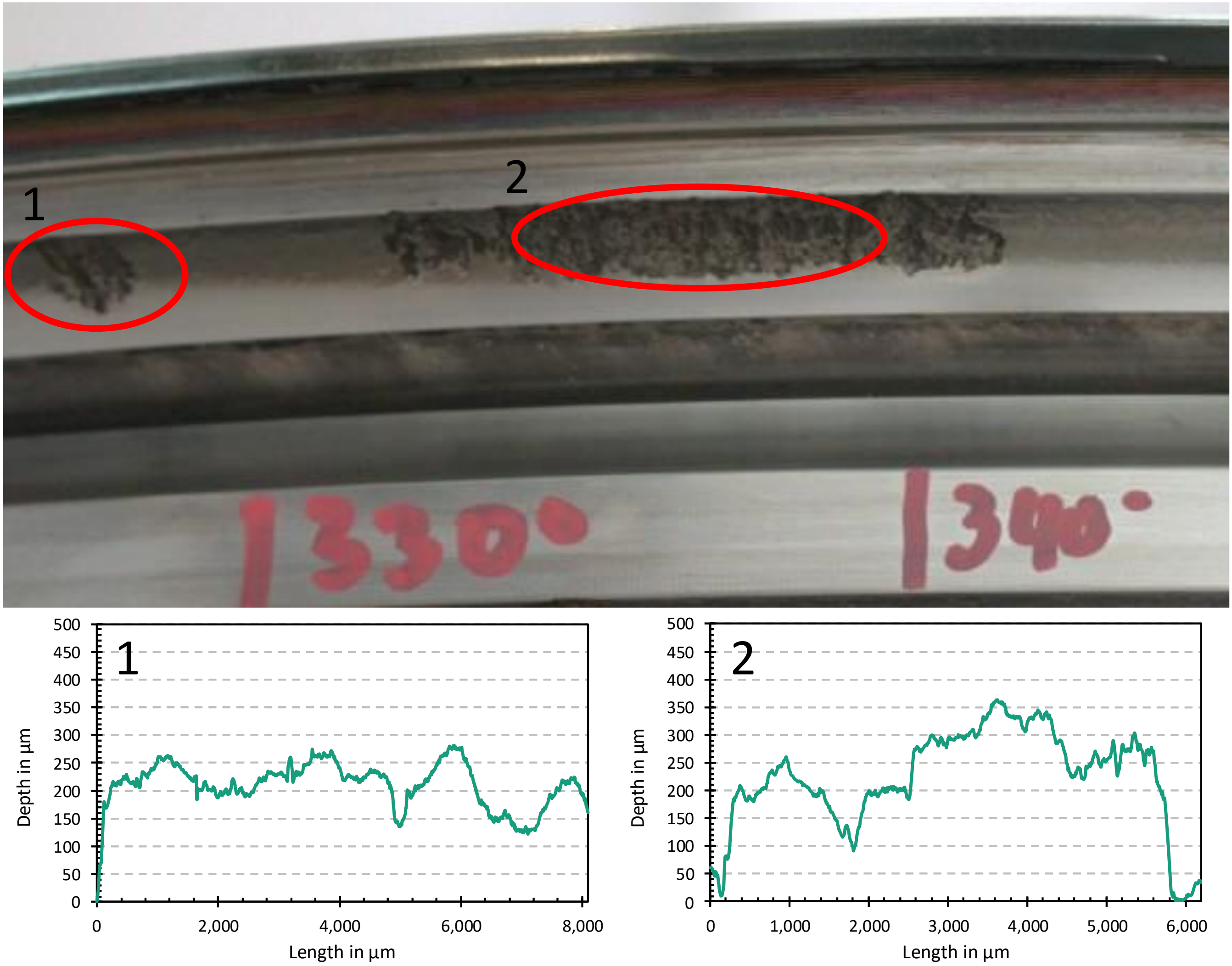


**Figure 10: Analysed damage marks of bearing 0411**

Figure 11 exemplarily shows the evaluation of two damage marks on the raceways of bearing 0498. The topology of the damage marks for this bearing is very comparable. However, for bearing 0498 the first plateau and therefore the first contact point with a ball is around 150 µm. Based on the results of the damage mark analysis, a gap of 200 µm for bearing 0411 and 150 µm for bearing 0498 is added to the springs in the FE bearing to consider the damage.

https://doi.org/10.5194/wes-2026-112
Preprint. Discussion started: 14 July 2026


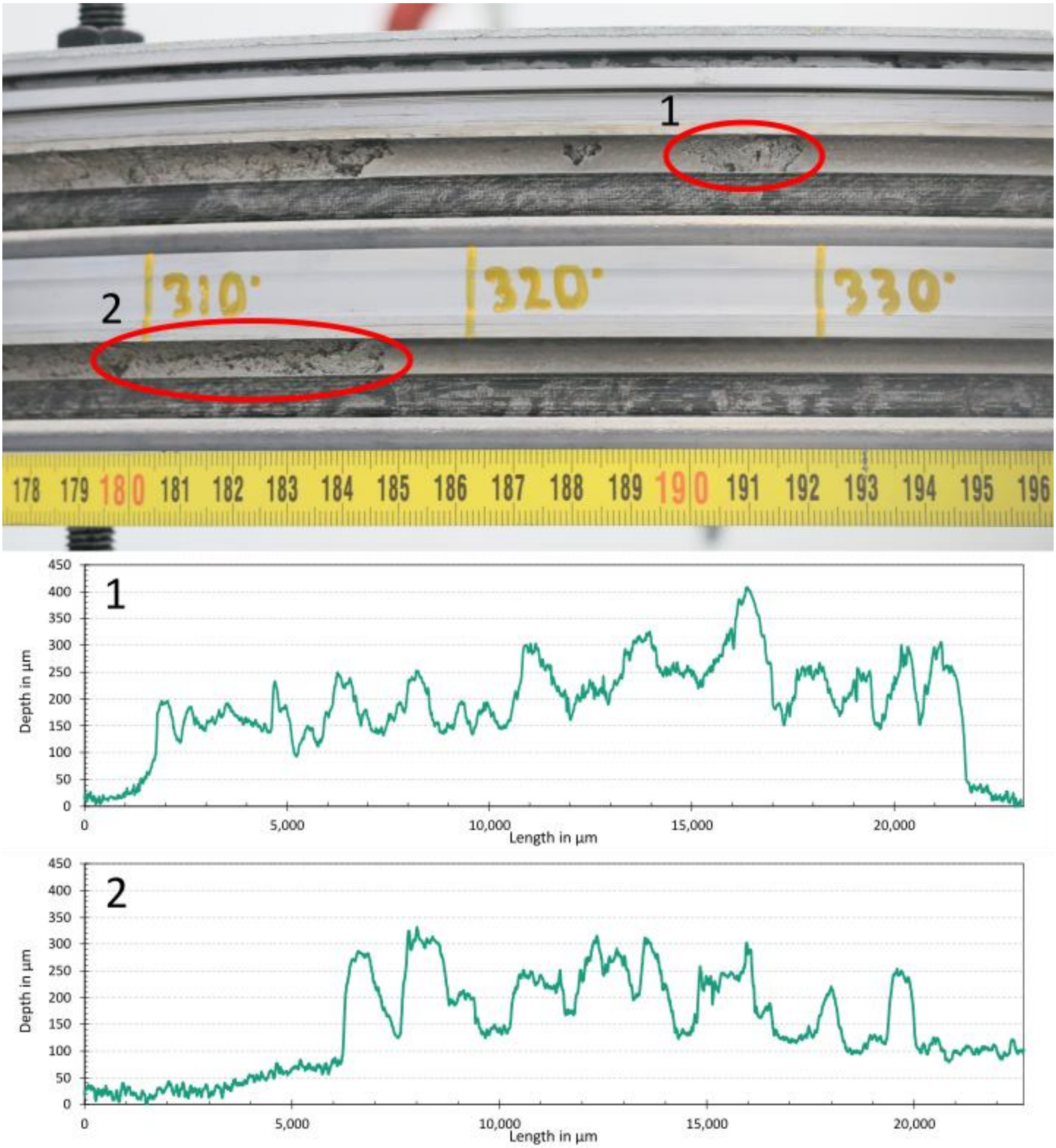


**Figure 11: Analysed damage marks of bearing 0498**

### 2.5 Bearing life calculation

In order to assess the effect of damages on the life, rolling contact fatigue life calculations of the bearing as per NREL DG03 (Stammler et al. 2024) which closely adheres to ISO 16281 (2008) were carried out. These include the altered load distributions of the bearings on a macroscopic scale that are discussed below. This means that the fact that some parts of the raceway carried a different load due to the macroscopic damage is considered. The different microscopic geometry of the raceway that would lead to a non-Hertzian, scattered contact distribution is not considered; rather, Hertzian contact is assumed wherever contact takes place. Furthermore, possible pressure increases due to truncation at entrance and leaving of the damage mark is neglected. This life calculation therefore aims to analyze the effect of global changes in the load distribution on the life of the bearing.

Rating life calculations are meant to predict the first visible onset of fatigue on the raceway of an intact bearing. Carrying out a life calculation of an already damaged bearing is therefore somewhat unusual. In the present case, the life calculated in this manner can be interpreted as the likelihood for a new damage to occur on the still intact locations of the raceway due to the global changes in the load distribution alone.

## 3 Results and discussion

### 3.1 Damage implementation

As shown in Figure 3, applying a negative displacement sets an offset to the springs that need to be compensated before the spring starts carrying load. Hence, applying a displacement of -200 µm or -150 µm to a spring-pretension combination represents the behavior of a ball raceway interaction with raceway damages of respectively 200 µm or 150 µm depth. Applying displacements for each spring-pretension combination individually allows for modelling every bearing condition shown in Figure 7 and Figure 8.

### 3.2 Model validation

Figure 12 shows the strain gauge data of bearing 0411 at different states during the fatigue tests visualizing changes in the bearing behavior due to damage progression. It starts with the initial undamaged state at the top left and continues with the different conditions that are documented during the disassemblies. All diagrams show the resulting strain in µm/m over the circumferential position of the bearing. The reference test rotates the inner ring of the bearing at a constant load level. That continuously changes interactions of particular segments on the inner and outer rings through the balls which results in many different separate deformation responses. Contrarily, the FE simulations, plotted in black, only consider the bearing behavior at one specific location without pitch movements. Hence, the minimum, maximum, and mean values of the experiment are shown in green in the diagrams to describe the bearing deformation with a range of data. During the multiple disassembling and reassembling processes some strain gauges got damaged explaining the missing data points in the diagrams. Especially

https://doi.org/10.5194/wes-2026-112
Preprint. Discussion started: 14 July 2026


WIND ENERGY SCIENCE DISCUSSIONS

towards the end of the test damaged strain gauges were not replaced due to limited time on the test rig. Comparing the experimental and simulative results show that the simulations fit the bearing behavior in most cases for all the different conditions. Only single outliers show smaller deviations from the range of experimental data. Table 2 lists the experimental and simulation strain at the positions 25° and 175°. At all positions, the deviation between the simulation and the range of experimental data is far below 10%. The largest deviations can be seen for the 5$^{th}$ disassembly, indicating a limitation of the modelling approach of implementing damage in the FE bearing model when too much area of the raceways is damaged. Figure 12 also shows that the behavior of the bearing outer ring changes over time due to increasing damage. Especially between 120° and 240° the characteristic of the strain changes. That is noticeable for the experiment as well as the simulation results. The characteristics of the simulation results noticeably change more than the experiment over time. That might be because the experimental data show results for a range of pitch positions while the FE data show results only for 0° position without pitching.

https://doi.org/10.5194/wes-2026-112
Preprint. Discussion started: 14 July 2026


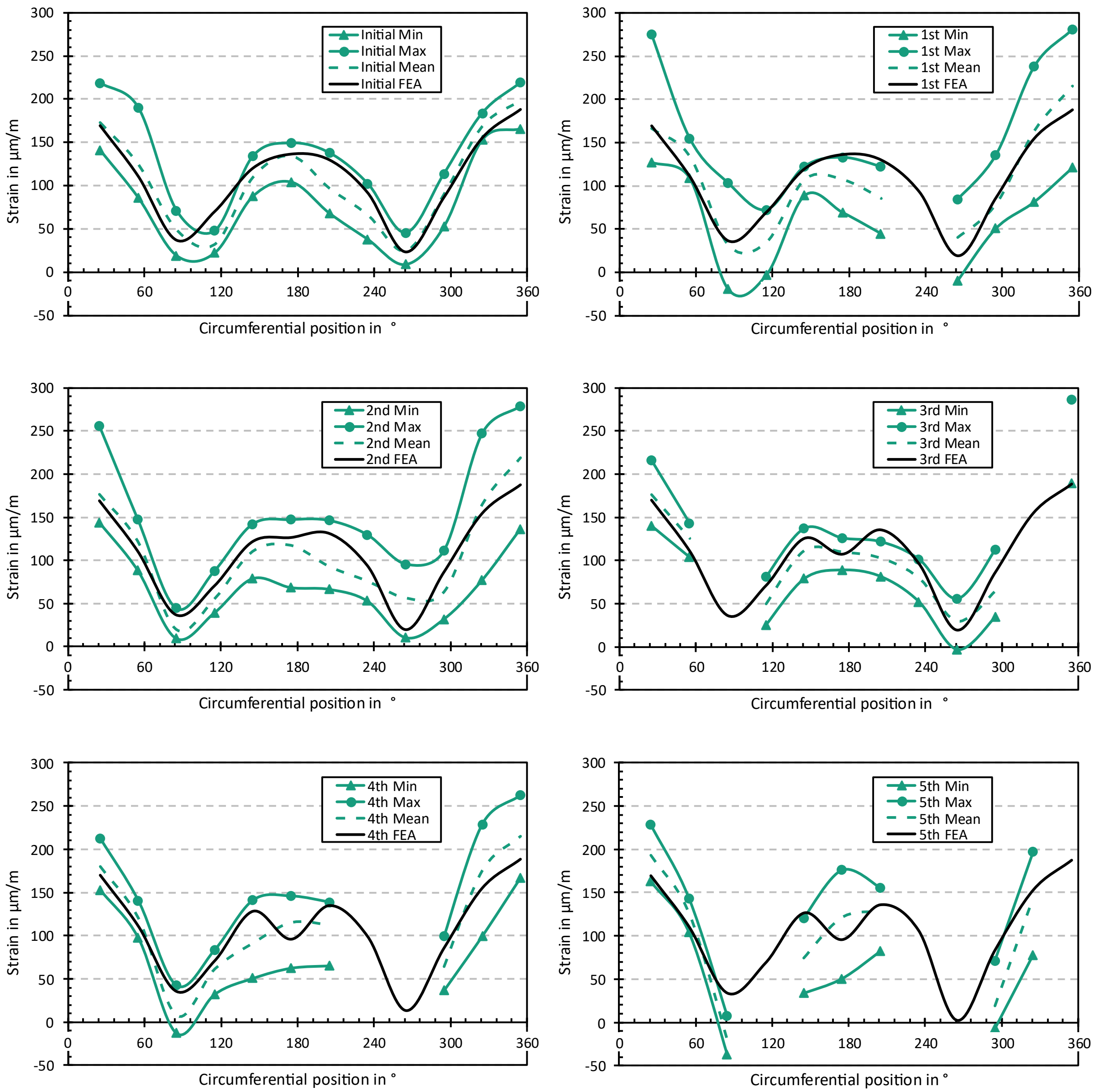


**Figure 12: Strain gauge data for bearing 0411 at different states**

**Table 2: Maximum experimental and simulation strain for bearing 0411 at different states**

| Disassembly | Position in ° | Experiment | | Simulation | |
|---|---|---|---|---|---|
| | | Minimum strain in µm/m | Maximum strain in µm/m | Strain in µm/m | Deviation from nearest measurement value in % |
| Initial | 25 | 141 | 218 | 169 | 0.00 |

https://doi.org/10.5194/wes-2026-112
Preprint. Discussion started: 14 July 2026


| | | | | | |
|---|---|---|---|---|---|
| | 175 | 104 | 149 | 136 | 0.00 |
| 1st | 25 | 127 | 275 | 169 | 0.00 |
| | 175 | 69 | 133 | 136 | 2.26 |
| 2nd | 25 | 144 | 256 | 169 | 0.00 |
| | 175 | 69 | 147 | 127 | 0.00 |
| 3rd | 25 | 155 | 223 | 170 | 0.00 |
| | 175 | 85 | 130 | 107 | 0.00 |
| 4th | 25 | 153 | 212 | 170 | 0.00 |
| | 175 | 62 | 146 | 96 | 0.00 |
| 5th | 25 | 163 | 228 | 170 | 0.00 |
| | 175 | 50 | 176 | 96 | 0.00 |

Figure 13 shows the strain gauge data for bearing 0498 at the initial state and with damage on the raceway after the fatigue test. Again, the range of experimental data is displayed in green and the FE results in black. The dashed black line shows the results for the FE model without any system preload like bearing 0411. As already mentioned in Section 2.1 the initial torque of bearing 0498 is significantly higher than for bearing 0411. This indicates a substantial tighter fit between the balls and raceways, resulting in greater system preload and leading to a stiffer bearing behavior and therefore less strain in the bearing rings compared to the bearing behavior without any preload. Finding the right preload value is an iterative process that needs to be done for each individual bearing as the fit between the balls and raceways change even within one batch of bearings. For the bearing in this study an optimum system preload of 60 µm was found. Hence, an offset of 60 µm is added to each spring-pretension combination. The straight black line shows the FE results considering the resulting system preload. When including the damage to the FE bearing model, the damage depth of 150 µm is subtracted from the initially added preload. The results show a very good fit of the simulation with the experiment when the system preload is considered in the FE model. It also shows a change in the characteristic of bearing behavior due to damage on the raceway. Table 3 lists the experiment and simulation strain at the positions 175° and 325°. It shows no deviations between the simulation and the range of experimental results.

https://doi.org/10.5194/wes-2026-112
Preprint. Discussion started: 14 July 2026


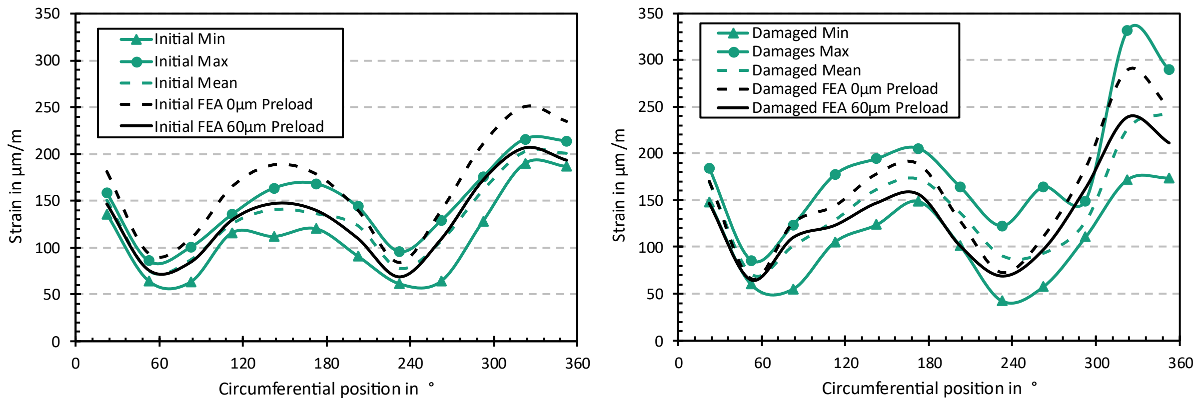


**Figure 13: Strain gauge data for bearing 0498 at initial and damaged states**

**Table 3: Maximum experimental and simulation strain for bearing 0498 at initial and damaged states**

| | Position in ° | Experiment | | Simulation | |
|---|---|---|---|---|---|
| | | Minimum strain in µm/m | Maximum strain in µm/m | Strain in µm/m | Deviation from nearest measurement value in % |
| Initial | 175 | 121 | 169 | 140 | 0.00 |
| | 325 | 190 | 216 | 207 | 0.00 |
| Damaged | 175 | 149 | 205 | 156 | 0.00 |
| | 325 | 172 | 331 | 239 | 0.00 |

### 3.3 Bearing life

When material is locally removed from the raceway the rolling element in that position is not carrying any load. Besides changes in the deformation of the bearing rings, that highly influences the load distribution among the balls in the bearing. When one or multiple balls next to each other are not carrying any load, the load on neighboring balls increases. That results in higher contact pressures and therefore reduces the bearing life. Figure 14 shows the ball forces for bearing 0411 for diagonal 1 in the blade side row on the left and diagonal 3 in the hub side row on the right for the axial loading of the fatigue test. The diagrams display the changes in the load distribution for all disassemblies starting with the initial state without any damage. The ball forces increase drastically with increasing damage. From the 4$^{th}$ disassembly on, the results also show that springs in damaged areas start carrying load again. That indicates that balls get back in touch with the damaged raceway once large areas of the raceways are damaged.

https://doi.org/10.5194/wes-2026-112
Preprint. Discussion started: 14 July 2026


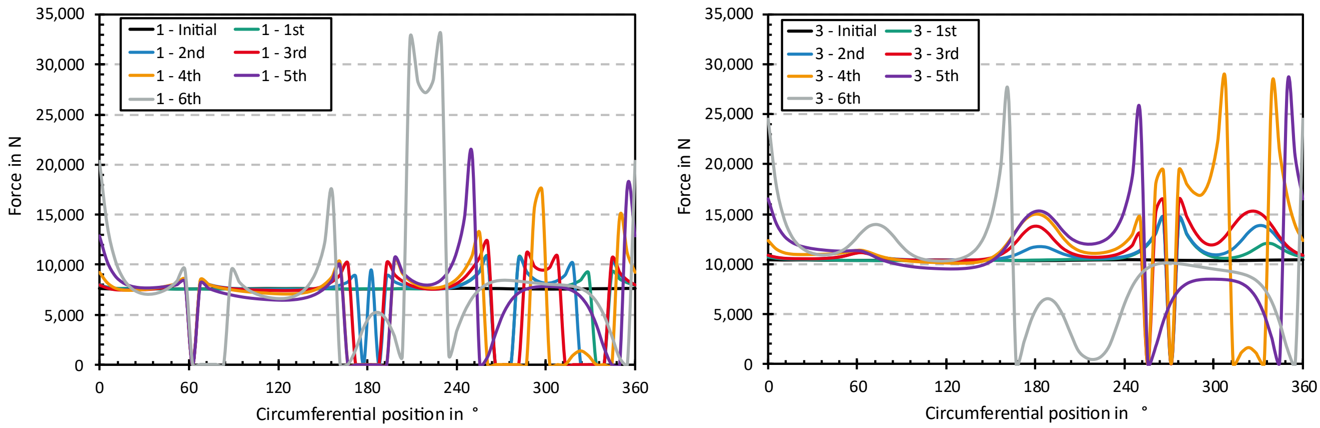


**Figure 14: Ball forces for bearing 0411 at different states for diagonal 1 (left) and diagonal 3 (right)**

The different load distributions lead to a different life, even with local effects in the surface roughness such as non-Hertzian contacts and truncation are neglected. Figure 15 shows the $L_{10}$ life calculated according to NREL DG03, in close adherence to ISO 16281, of an otherwise identical new bearing with the new load distributions shown in Figure 14. On the abscissa, the equivalent number of test rotations at which the disassemblies took place are shown. As less and less of the bearing circumference carries load, the $L_{10}$ life can be seen to decrease more and more, because balls that still carry load need to compensate for those that cannot carry load due to local spalls; this leads to increased Hertzian pressure for the balls that still carry load, which reduces the theoretical life of the bearing. Only for disassembly 5, there appears to be an anomaly, as the life increases as compared to disassembly 4. This is due to the fact that for disassembly 5, the bearing has sustained so much damage, and therefore experiences so much additional rigid body movement, that balls start to carry load again in locations in which they previously could not carry load due to the spalling. This leads to a brief improvement of the global load distribution, which in turn positively affects the life. This effect is only of a brief duration, however, as disassembly 6 obtains the lowest of all lives, despite the fact that local surface changes are neglected in this calculation, which would have an even more detrimental effect on the life of the bearing.

The calculations therefore indicate that the altered global load distribution has a negative effect on the remaining useful life: As the rating life goes down significantly, new damages are much more likely to form on the raceway due to the changed global load distribution, neglecting other effects.

https://doi.org/10.5194/wes-2026-112
Preprint. Discussion started: 14 July 2026


Open Access
WIND ENERGY SCIENCE DISCUSSIONS

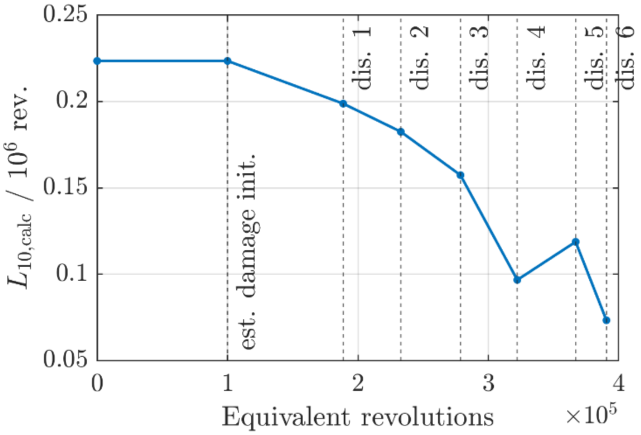


**Figure 15: Calculated $L_{10}$ life for the different macroscopic load distributions of bearing 0411**

Figure 16 shows the ball forces for bearing 0498 with and without damage on the raceway. Again, the maximum load in the bearing significantly increases with damage on the raceway.

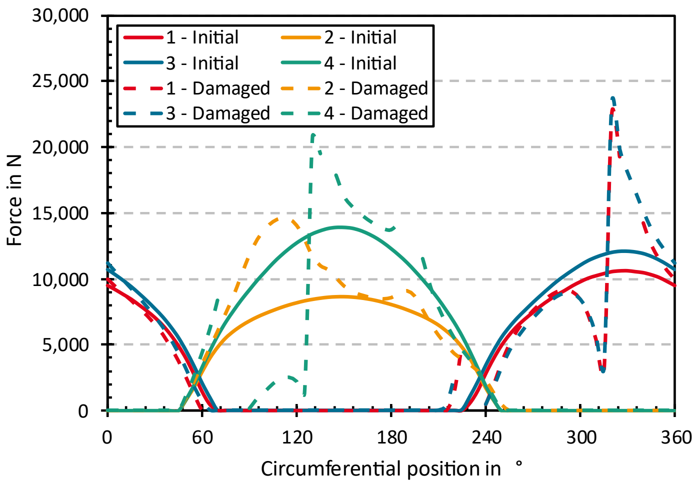


**Figure 16: Ball forces for bearing 0498 at initial and damaged states**

Again, the $L_{10}$ lives of an intact bearing with the same load distribution as those shown in Figure 16 were calculated. They are shown in Figure 17. Similar to bearing 0411, as the damage in the bearing increases, the life can be seen to go down, indicating that new damages are somewhat more likely to form due to the changes in the load distribution of the bearing.

https://doi.org/10.5194/wes-2026-112
Preprint. Discussion started: 14 July 2026


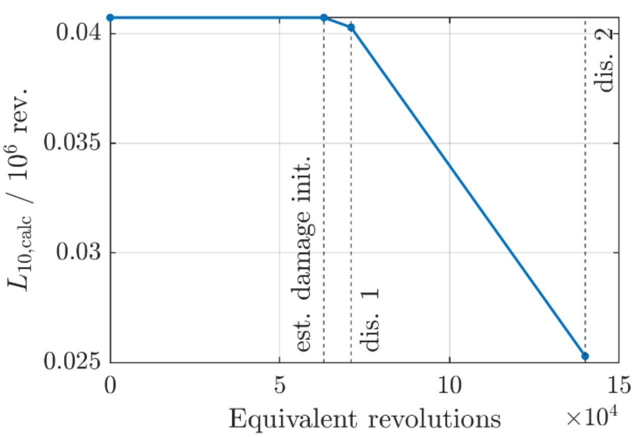


**Figure 17: Calculated $L_{10}$ life for the different macroscopic load distributions of bearing 0498**

## 4 Conclusion

This work has implemented raceway damage in the finite-element model of downscaled blade bearings of a wind turbine to investigate changes in the bearing behavior. The bearings are double-row four-point contact ball bearings with same material and manufacturing process as original-sized blade bearings. To enhance computational efficiency, the ball–raceway interactions are represented by nonlinear spring elements. To implement damage, pretension elements that can introduce gaps are added to springs creating spring-pretension combinations.

The proposed modelling approach to capture changes in the deformation behavior of the bearing caused by raceway damage has been successfully validated against experimental data. The comparison of simulation results with experimental strain gauge data has shown that the deviation of the maximum strain at different states of raceway damage always is below 10%. For most investigated conditions, the FE results agree well with the experimental measurements and reproduce the characteristic changes in the strain distribution along the circumference, fulfilling the defined validation criteria. Larger deviations were observed only for very advanced damage states, indicating limitations of the simplified damage representation when large portions of the raceway are affected. The results demonstrate that local material removal on the raceway leads to significant changes in the global load distribution. Balls located in damaged areas temporarily lose contact, resulting in increased loads on neighboring balls. As damage increases, the global bearing deformation also increases significantly, leading to renewed contact between the balls and the damaged parts of the raceway. Consequently, the calculated $L_{10}$ life decreases substantially with progressing damage, highlighting that the altered load distribution alone already increases the likelihood of further damage initiation. Overall, the study shows that incorporating raceway damage into FE bearing models provides valuable insight into the evolving load distribution and its influence on the calculated bearing life. This is essential for a more realistic assessment of damaged bearings in operation and generally understanding damage progression in wind turbine blade bearings.

Future work will focus on improving the representation of damage by introducing more advanced models with spatially varying gap offsets and considering multiple damage geometries and locations. Furthermore, the influence of the altered surface microgeometry and truncation at the edges of damage marks on the calculated bearing life will be investigated.

## Data availability

Data will be made available on request.

## Author contributions

MG: conceptualization, methodology, validation, writing (original draft). OM: investigation, writing (review and editing). AK: methodology. FS: writing (review and editing).

## Competing interests

The contact author has declared that none of the authors has any competing interests.

## Acknowledgements

The authors gratefully acknowledge the contribution of Matthias Stammler for internally reviewing this work. Copilot was used to optimize the text structure in some sections.

## Financial support

This research has been supported by the German Federal Ministry for Economic Affairs and Climate Action (grant no. 03EE3065 and 03EE3091A).

https://doi.org/10.5194/wes-2026-112
Preprint. Discussion started: 14 July 2026


## References

Aguirrebeitia, J.; Abasolo, M.; Avilés, R.; Fernández de Bustos, I.: General static load-carrying capacity for the design and selection of four contact point slewing bearings: Finite element calculations and theoretical model validation. In *Finite Elements in Anal. and Des.* 55, pp. 23–30. DOI: 10.1016/j.finel.2012.02.002, 2012.

Aithal, S.; Siva Prasad., N.; Shunmugam, M. S.; Chellapandi, P.: Effect of manufacturing errors on load distribution in large diameter slewing bearings of fast breeder reactor rotatable plugs. In *Proc IMechE Part C: J. Mech. Eng. Sci.* 230 (9), pp. 1449–1460. DOI: 10.1177/0954406215579947, 2012.

Arakere, N. K.; Branch, N.; Levesque, G.; Svendsen, V.; Forster, N. H.: Rolling Contact Fatigue Life and Spall Propagation of AISI M50, M50NiL, and AISI 52100, Part II: Stress Modeling. In *Tribology Transactions* 53 (1), pp. 42–51. DOI: 10.1080/10402000903226325, 2009.

Behnke, K.; Menck, O.: Rolling contact fatigue tests on pre-damaged slewing bearings. In *Proceedings of the Institution of Mechanical Engineers, Part J: Journal of Engineering Tribology*, Article 13506501251385051. DOI: 10.1177/13506501251385051, 2025.

Branch N. A., Arakere N. K., Svendsen V., Forster N. H.: Stress Field Evolution in a Ball Bearing Raceway Fatigue Spall. In *Journal of ASTM International* 7 (2), pp. 1–18. DOI: 10.1520/JAI102529, 2010.

Chen, G.; Wen, J.: Load Performance of Large-Scale Rolling Bearings with Supporting Structure in Wind Turbines. In *J. of Tribol.* 134 (4), Article 041105, p. 1087. DOI: 10.1115/1.4007349, 2012.

Daidié, A.; Chaib, Z.; Ghosn, A.: 3D Simplified Finite Elements Analysis of Load and Contact Angle in a Slewing Ball Bearing. In *J. Mech. Des.* DOI: 10.1115/1.2918915, 2008.

Gao, X. H.; Huang, X. D.; Wang, H.; Chen, J.: Modelling of ball-raceway contacts in a slewing bearing with non-linear springs. In *J. Mech. Eng. Sci.* 225 (4), pp. 827–831. DOI: 10.1177/09544062JMES2454, 2011.

Golmohammadi, Z.; Walvekar, A.; Sadeghi, F.: A 3D efficient finite element model to simulate rolling contact fatigue under high loading conditions. In *Tribology International* 126, pp. 258–269. DOI: 10.1016/j.triboint.2018.05.029, 2018.

Graßmann, M.; Geibel, M.; Schleich, F.: Validation of a finite-element model of a 5 m three-row roller wind turbine blade bearing. In *Wind Energ. Sci.* 11 (1), pp. 251–264. DOI: 10.5194/wes-11-251-2026, 2026.

https://doi.org/10.5194/wes-2026-112
Preprint. Discussion started: 14 July 2026


Graßmann, M.; Schleich, F.; Stammler, M.: Validation of a finite-element model of a wind turbine blade bearing. In *Finite Elements in Anal. and Des.* 221, p. 103957. DOI: 10.1016/j.finel.2023.103957, 2023.

Graßmann, M.; Stammler, M.; Menck, O.; Schleich, F.: The influence of anomalies in supporting structures on the validation of finite-element blade bearing models. In *Finite Elements in Anal. and Des.* 242, p. 104268. DOI: 10.1016/j.finel.2024.104268, 2024.

Heras, I.; Aguirrebeitia, J.; Abasolo, M.; Coria, I.: Load Distribution in Four-Point Contact Slewing Bearings Considering Manufacturing Errors and Ring Flexibility. In Burkhard Corves, Mathias Hüsing, Philippe Wenger (Eds.): EuCoMeS 2018. Proceedings of the 7th European Conference on Mechanism Science, vol. 59. European Conference on Mechanism Science. 1st ed. 2019. Cham: Springer International Publishing; Imprint: Springer (Mechanisms and Machine Science, 59), pp. 267–274, 2019a.

Heras, I.; Aguirrebeitia, J.; Abasolo, M.; Coria, I.; Escanciano, I.: Load distribution and friction torque in four-point contact slewing bearings considering manufacturing errors and ring flexibility. In *Mech. and Mach. Theory* 137, pp. 23–36. DOI: 10.1016/j.mechmachtheory.2019.03.008, 2019b.

ISO/TS 16281:2008 + Cor. 1:2009: Rolling bearings – Methods for calculating the modified reference rating life for universally loaded bearings, 2008.

Kotzalas, M. N.; Harris, T. A.: Fatigue Failure Progression in Ball Bearings. In *Journal of Tribology* 123 (2), pp. 238–242. DOI: 10.1115/1.1308013, 2001.

Liu, R.; Wang, H.; Pang, B. T.; Gao, X. H.; Zong, H. Y.: Load Distribution Calculation of a four-Point-Contact Slewing Bearing and its Experimental Verification. In *Exp. Tech.* 42 (3), pp. 243–252. DOI: 10.1007/s40799-018-0237-2, 2018.

Menck, O.; Geibel, M.: Service life of roller and ball pitch bearings in wind turbines: two examples. Wind Bearing Forum, Hamburg, 23 September 2025, 2025.

Ohana, R.; Klein, R.; Shneck, R.; Bortman, J.: Experimental Investigation of the Spall Propagation Mechanism in Bearing Raceways. In *Materials* 16 (1), p. 68. DOI: 10.3390/ma16010068, 2022.

Potočnik, R.; Göncz, P.; Glodež, S.: Static capacity of a large double row slewing ball bearing with predefined irregular geometry. In *Mech. and Mach. Theory* 64, pp. 67–79. DOI: 10.1016/j.mechmachtheory.2013.01.010, 2013.

Rosado, L.; Forster, N. H.; Thompson, K. L.; Cooke, J. W.: Rolling Contact Fatigue Life and Spall Propagation of AISI M50, M50NiL, and AISI 52100, Part I: Experimental Results. In *Tribology Transactions* 53 (1), pp. 29–41. DOI: 10.1080/10402000903226366, 2009.

Rumbarger, J. H.: Evaluation of the Life Margin of Oscillating Needle Roller Bearings. In *A S L E Transactions* 12 (2), pp. 162–170. DOI: 10.1080/05698196908972258, 1969.

Shen, F.; Zhou, K.: An elasto-plastic-damage model for initiation and propagation of spalling in rolling bearings. In *International Journal of Mechanical Sciences* 161-162, p. 105058. DOI: 10.1016/j.ijmecsci.2019.105058, 2019.

Singh, S.; Howard, C. Q.; Hansen, C. H.; Köpke, U. G.: Analytical validation of an explicit finite element model of a rolling element bearing with a localised line spall. In *Journal of Sound and Vibration* 416, pp. 94–110. DOI: 10.1016/j.jsv.2017.09.007, 2018.

Singh, S.; Köpke, U. G.; Howard, C. Q.; Petersen, D.: Analyses of contact forces and vibration response for a defective rolling element bearing using an explicit dynamics finite element model. In *Journal of Sound and Vibration* 333 (21), pp. 5356–5377. DOI: 10.1016/j.jsv.2014.05.011, 2014.

Slack, T.; Sadeghi, F.: Explicit finite element modeling of subsurface initiated spalling in rolling contacts. In *Tribology International* 43 (9), pp. 1693–1702. DOI: 10.1016/j.triboint.2010.03.019, 2010.

Smolnicki, T.; Rusiński, E.: Superelement-Based Modeling of Load Distribution in Large-Size Slewing Bearings. In *J. Mech. Des.* 129 (4), pp. 459–463. DOI: 10.1115/1.2437784, 2007.

Stammler, M.; Baust, S.; Reuter, A.; Poll, G.: Load distribution in a roller-type rotor blade bearing. In *J. Phys.: Conf. Ser.* 1037. DOI: 10.1088/1742-6596/1037/4/042016, 2018.

Stammler, M.; Menck, O.; Guo, Y.; Keller, J.: Wind Turbine Design Guideline DG03: Yaw and Pitch Bearings. Golden, CO: National Renewable Energy Laboratory. NREL/TP-5000-89161. https://www.nrel.gov/docs/fy24osti/89161.pdf, 2024.

Starvin, M. S.; Manisekar, K.: The effect of manufacturing tolerances on the load carrying capacity of large diameter bearings. In *Sadhana* 40, pp. 1899–1911. DOI: 10.1007/s12046-015-0427-x, 2015.

Walvekar, A. A.; Morris, D.; Golmohammadi, Z.; Sadeghi, F.; Correns, M.: A Novel Modeling Approach to Simulate Rolling Contact Fatigue and Three-Dimensional Spalls. In *Journal of Tribology* 140 (3), Article 031101, p. 31101. DOI: 10.1115/1.4038098, 2018.

Walvekar, A. A.; Paulson, N.; Sadeghi, F.; Weinzapfel, N.; Correns, M.; Dinkel, M.: A New Approach for Fatigue Damage Modeling of Subsurface-Initiated Spalling in Large Rolling Contacts. In *Journal of Tribology* 139 (1), Article 011101, p. 11101. DOI: 10.1115/1.4033054, 2017.

Wang, H.; He, P.; Pang, B.; Gao, X.: A new computational model of large three-row roller slewing bearings using nonlinear springs. In *J. Mech. Eng. Sci.* 231 (20), pp. 3831–3839. DOI: 10.1177/0954406217704223, 2017.